Divergent versus Nondivergent Instabilities of Piecewise Uniform Shear Flows on the *f* Plane

NATHAN PALDOR

Institute of Earth Sciences, The Hebrew University of Jerusalem, Jerusalem, Israel

YONA DVORKIN

Geological Survey of Israel, Jerusalem, Israel

EYAL HEIFETZ

Department of Geophysics and Planetary Sciences, Tel Aviv University, Tel Aviv, Israel

(Manuscript received 6 May 2008, in final form 16 January 2009)

ABSTRACT

The linear instability of a piecewise uniform shear flow is classically formulated for nondivergent perturbations on a 2D barotropic mean flow with linear shear, bounded on both sides by semi-infinite half-planes where the mean flows are uniform. The problem remains unchanged on the *f* plane because for nondivergent perturbations the instability is driven by vorticity gradient at the edges of the inner, linear shear region, whereas the vorticity itself does not affect it. The instability of the unbounded case is recovered when the outer regions of uniform velocity are bounded, provided that these regions are at least twice as wide as the inner region of nonzero shear. The numerical calculations demonstrate that this simple scenario is greatly modified when the perturbations' divergence and the variation of the mean height (which geostrophically balances the mean flow) are retained in the governing equations. Although a finite deformation radius exists on the shallow water *f* plane, the mean vorticity gradient that governs the instability in the nondivergent case remains unchanged, so it is not obvious how the instability is modified by the inclusion of divergence in the numerical solutions of the equations. The results here show that the longwave instability of nondivergent flows is recovered by the numerical solution for divergent flows only when the radius of deformation is at least one order of magnitude larger than the width of the inner uniform shear region. Nevertheless, even at this large radius of deformation both the amplitude of the velocity eigenfunction and the distribution of vorticity and divergence differ significantly from those of nondivergent perturbations and vary strongly in the cross-stream direction. Whereas for nondivergent flows the vorticity and divergence both have a delta-function structure located at the boundaries of the inner region, in divergent flows they are spread out and attain their maximum away from the boundaries (either in the inner region or in the outer regions) in some range of the mean shear. In contrast to nondivergent flows for which the mean shear is merely a multiplicative factor of the growth rates, in divergent flows new unstable modes exist for sufficiently large mean shear with no shortwave cutoff. This unstable mode is strongly affected by the sign of the mean shear (i.e., the sign of the mean relative vorticity).

1. Introduction

Mean flows with uniform shear on an infinite plane constitute a prime example of a stable flow, as can be easily shown by studying the corresponding Rayleigh equation. The obvious reason for this is that the mean vorticity gradient in such mean flows vanishes, so it cannot satisfy the ''inflection point'' necessary condition for instability that requires the mean vorticity gradient to change sign somewhere in the domain (Pedlosky 1987). The stability of these flows is easily demonstrated for nondivergent, small-amplitude perturbations for which the vorticity vanishes so that its evolution equation reduces to Laplace's equation for the streamfunction ψ (see, e.g., Cushman-Roisin 1994):

Corresponding author address: Nathan Paldor, Institute of Earth Sciences, The Hebrew University of Jerusalem, Jerusalem 91904, Israel.
E-mail: nathan.paldor@huji.ac.il

DOI: 10.1175/2009JPO4048.1

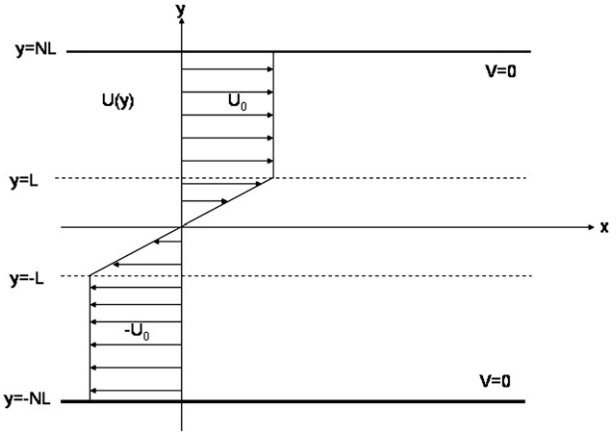

FIG. 1. The flow with piecewise uniform shear. In Rayleigh's classical (unbounded) theory the inner region ($-L < y < L$) where $U(y) = yU_0/L$ is imbedded within two outer half-planes in which $U(y) = U_0$. In the finite case, two walls are placed in the outer regions at $y = \pm NL$ ($N > 1$).

$$\nabla^2\psi = 0. \tag{1.1}$$

The addition of uniform rotation to the dynamics does not alter Eq. (1.1) because the mean vorticity gradient remains zero. However, when the shear zone is bounded by two half-planes where the velocity is uniform (see Fig. 1), instabilities arise from the discontinuity of the mean flow's shear (U_0/L), which results in a jump condition for the perturbations' tangential velocity. The mean vorticity gradient is concentrated in two δ functions with opposite sign at the edges of the shear zone so that Rayleigh instability criterion is satisfied at these points. The unstable modes result from the far-field (action at a distance) interaction between two counterpropagating Rossby vorticity edge waves that are phase-locked in a growing configuration (e.g., Heifetz et al. 1999).

It should be noted that the continuous spectrum is filtered out in the derivation of Eq. (1.1) (see Case 1960) so transient temporal growth of the perturbations (Farrell 1988) is not possible.

Solving Eq. (1.1) for a wave in x and t [so $\psi \sim e^{i(kx-Ct)}$] yields exponential variation of $\psi(y)$, which decays exponentially in the two outer regions and is a combination of $\sinh(ky)$ and $\cosh(ky)$ in the inner region. The jump condition of $u = -d\psi/dy$ at the boundaries $y = \pm L$ (which introduces explicit time variation into the problem) yields the dispersion relation (see Cushman-Roisin 1994; Drazin and Reid 1981):

$$\left(\frac{kCL}{U_0}\right)^2 = \left(\frac{1}{2} - kL\right)^2 - \frac{1}{4}e^{-4kL}. \tag{1.2}$$

The phase speed C in this dispersion relation is imaginary for $0 < kL < 0.639$ and the maximal growth rate of $kLC_i/U_0 = 0.2$ is located at $kL = 0.4$. The graph of $kC(k)$ in this nondivergent (ND) case is shown in the solid curve of Fig. 2. It is clear from Eq. (1.2) that the mean shear ω ($= U_0/L$) multiplies the growth rate curve $kC(k)$ but does not alter its shape.

When the outer regions are bounded and do not extend to infinity (i.e., U is uniform in the two outer regions $L < |y| < NL$, where $N > 1$ is an arbitrary number), the solutions in these regions are given by linear combinations of $\sinh(ky)$ and $\cosh(ky)$. A straightforward analysis of the resulting complicated expression for the phase speed (Drazin and Reid 1981, section 23) shows that the perturbations are unstable for $N > 2$.

The above results were derived for nondivergent perturbations where both the mean velocity and the perturbation velocity are decoupled from the height field and the pressure that forces the velocity is applied (in an undetermined way) by a "rigid lid" that is assumed to overlie the fluid. The relevance of nondivergent theories to divergent flows is not obvious, and an example in which it could be convincingly demonstrated that divergent instabilities do not constitute regular limits of the associated nondivergent instabilities is the zonal $\cos^2$ jet. This jet is the primary example of barotropic instability theory studied by Kuo (1973) but, as shown by Paldor and Dvorkin (2006), the shortwave cutoff that typifies the nondivergent theory is completely absent in the divergent case. This addition of horizontal divergence of the horizontal velocity implies that the pressure is determined hydrostatically by the fluid height (instead of being applied by the rigid lid), which varies in time in response to the divergence of the horizontal velocity. As for the equations themselves (and not their solutions) Paldor (2008) has shown that in the absence of a mean flow, the nondivergent equations constitute a regular limit of the associated divergent equations when the mean height becomes large, but only for very specific scaling of the variables.

In the absence of rotation, the effect of divergence on the type of dominant instability was demonstrated by Satomura (1981) and Balmforth (1999), who showed that an increase of the Froude number leads to the appearance of a gravity wave critical level instability (designated by Satomura as "super-sonic" instability) over Rossby-wave Rayleigh inflectional instability. As was pointed out above, in the nondivergent case of the piecewise linear shear of Fig. 1 the inflectional instability is the only source for modal growth, regardless of whether or not rotation is included. Hence, here we consider this simple setup

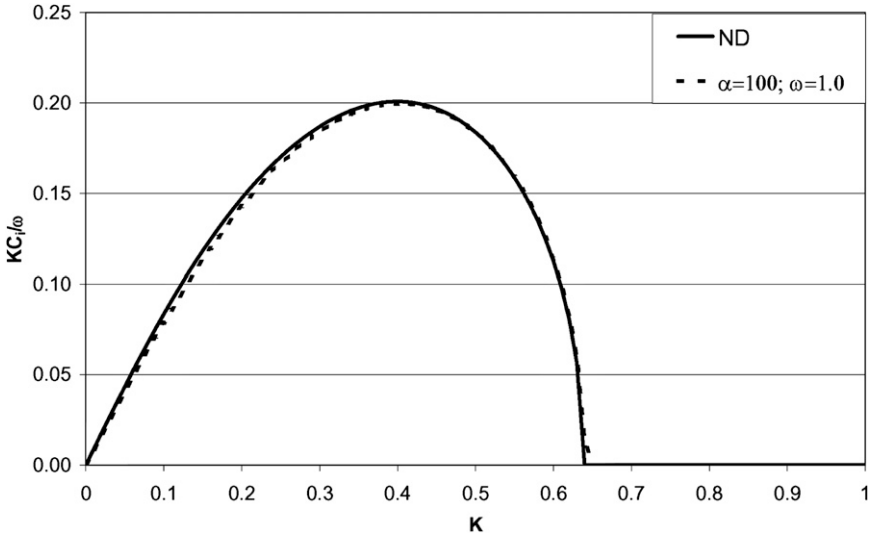

FIG. 2. Growth rate curves for ND and for the divergent perturbations with $\alpha = 100, \omega = 1$. The ND growth rates are very close to the divergent ones at these values of α and ω.

to combine the various elements discussed by Satomura (1981), Balmforth (1999), and Paldor (2008).

For unstable flows it is demonstrated that the addition of divergence limits the wavenumber range of instability and reduces the maximal growth rate. In rotating, quasigeostrophic (QG) flows, Pratt and Pedlosky (1991) showed that for velocity disturbances that are in geostrophic (but time-dependent) balance with the hydrostatic pressure, the Rayleigh instability prevails and its growth rate curve is qualitatively similar to that of the ND curve of Fig. 2.

Numerous observations of growing perturbations in the ocean were interpreted in terms of shear instability (e.g., Send 1989; Feng and Wijffels 2002), which highlights the crucial role played by this instability in time-dependent flows. The focus of this study is on normal mode analysis and not on transient instability (Farrell 1988). As we shall see, the relation between the divergent and nondivergent instabilities is not simple and depends on the wavenumber.

2. Formulation of the problem

Because our aim is to compare the Rayleigh instability in divergent and nondivergent flows, we formulate the mathematical problem so as to maintain the same set of equations in both cases. Accordingly, consider a mean zonal flow $U(y)$ on the f plane that has uniform shear in the intermediate region $-L < y < L$, which is embedded in a longitudinal channel of width $2NL$ (where the value of the number $N > 1$ is yet to be determined). The unperturbed (mean) velocity distribution in the channel is given by

$$U(y) = \begin{cases} -\omega L, & -NL \le y < -L \\ \omega y, & -L \le y < L \\ \omega L, & L \le y \le NL \end{cases},$$

$$\frac{dU}{dy} = \begin{cases} 0, & -NL \le y < -L \\ \omega, & -L \le y < L \\ 0, & L \le y \le NL \end{cases}, \tag{2.1}$$

where ω is a frequency representing the shear of $U(y)$ in the intermediate region (see Fig. 1).

The momentum and continuity equations of the shallow water model are

$$\frac{\partial(U+u)}{\partial t} + (U+u)\frac{\partial(U+u)}{\partial x} + v\frac{\partial(U+u)}{\partial y} - fv + g\frac{\partial(H+\eta)}{\partial x} = 0, \tag{2.2a}$$

$$\frac{\partial v}{\partial t} + (U+u)\frac{\partial v}{\partial x} + f(U+u) + g\frac{\partial(H+\eta)}{\partial y} = 0, \tag{2.2b}$$

$$\frac{\partial(H+\eta)}{\partial t} + \frac{\partial}{\partial x}[(H+\eta)(U+u)] + \frac{\partial}{\partial y}[(H+\eta)v] = 0, \tag{2.2c}$$

where $u(x, y, t)$ and $v(x, y, t)$ are the perturbation velocity components in the east x and north y directions, respectively; f is the Coriolis parameter; g is the (reduced) gravity; $H(y)$ is the mean height of the layer of fluid; and $\eta(x, y)$ is the perturbation's height. The lowest-order terms (i.e., zeroth-order terms in the perturbations' amplitude) in Eq. (2.2b) yield the geostrophic balance,

$$fU = -g\frac{\partial H}{\partial y}, \tag{2.3}$$

which implies that the height profile corresponding to the mean velocity (2.1) is

$$H(y) = \begin{cases} H_0 + \dfrac{f}{g}\omega L\left(\dfrac{L}{2} + y\right), & -NL \le y < -L \\ H_0 - \dfrac{f}{g}\omega\dfrac{y^2}{2}, & -L \le y < L \\ H_0 + \dfrac{f}{g}\omega L\left(\dfrac{L}{2} - y\right), & L \le y \le NL \end{cases}, \tag{2.4}$$

$$\frac{\partial H}{\partial y} = \begin{cases} \dfrac{f}{g}\omega L, & -NL \le y < -L \\ -\dfrac{f}{g}\omega y, & -L \le y < L \\ -\dfrac{f}{g}\omega L, & L \le y \le NL \end{cases},$$

where $H_0 = H(y = 0)$ is the largest value of $H(y)$. Linearization of system (2.2) yields

$$\frac{\partial u}{\partial t} + U\frac{\partial u}{\partial x} + v\frac{\partial U}{\partial y} - fv + g\frac{\partial \eta}{\partial x} = 0, \tag{2.5a}$$

$$\frac{\partial v}{\partial t} + U\frac{\partial v}{\partial x} + fu + g\frac{\partial \eta}{\partial y} = 0, \tag{2.5b}$$

$$\frac{\partial \eta}{\partial t} + U\frac{\partial \eta}{\partial x} + H\left(\frac{\partial u}{\partial x} + \frac{\partial v}{\partial v}\right) + v\frac{\partial H}{\partial y} = 0. \tag{2.5c}$$

We look for zonally propagating wave solutions $(u, v, \eta) = [u^*(y), v^*(y), \eta^*(y)]e^{ik(x-Ct)}$ (where C is the wave's phase speed and k is its wavenumber, so its frequency is kC) for which system (2.5) implies that (dropping the asterisks from the amplitudes)

$$u(U - C) + (U_y - f)V + g\eta = 0, \tag{2.6a}$$

$$-V(U - C)k^2 + fu + g\eta_y = 0, \tag{2.6b}$$

$$\eta(U - C) + H(u + V_y) + H_y V = 0, \tag{2.6c}$$

where the subscript y means differentiation with respect to y and where

$$V = \frac{v}{ik} = -\frac{iv}{k}. \tag{2.7}$$

Using Eq. (2.6a) to eliminate η from (2.6b) and (2.6c), we get the second-order differential system for (u, V):

$$u_y = \frac{(f - U_y)(U - C)}{gH}u - \left[\frac{U_{yy}}{U - C} + k^2 + \frac{(f - U_y)^2}{gH} + \frac{H_y}{H}\frac{f - U_y}{U - C}\right]V, \tag{2.8a}$$

$$V_y = \left[\frac{(U - C)^2}{gH} - 1\right]u - \left[\frac{(U - C)(f - U_y)}{gH} + \frac{H_y}{H}\right]V. \tag{2.8b}$$

To reduce the number of parameters in the problem, we nondimensionalize Eqs. (2.8) using L as the length scale of the x and y coordinates and $1/f$ as the time scale, so the velocity scale is fL (and the scale for $V \sim v/k$ is fL^2). For the height scale we use H_0 (the unperturbed fluid height at $y = 0$) and these scales yield the nondimensional counterpart of system (2.8):

$$u_y = \frac{(U - C)(1 - U_y)}{\alpha H}u - \left[k^2 + \frac{U_{yy}}{U - C} + \frac{(1 - U_y)^2}{\alpha H} + \frac{1 - U_y}{U - C}\frac{H_y}{H}\right]V, \tag{2.9a}$$

$$V_y = \left[\frac{(U - C)^2}{\alpha H} - 1\right]u - \left[\frac{(U - C)(1 - U_y)}{\alpha H} + \frac{H_y}{H}\right]V, \tag{2.9b}$$

where $\alpha = gH_0/f^2L^2$ is the square of the nondimensional speed of gravity waves (i.e., the Burger number and the inverse of Lamb's number). The nondimensional form of the mean state equations [(2.1) and (2.4)] is

$$U(y) = \begin{cases} -\omega, & -N \le y \le -1 \\ \omega y, & -1 \le y \le 1 \\ \omega, & 1 \le y \le N \end{cases};$$

$$H(y) = \begin{cases} 1 + \dfrac{\omega}{2\alpha}(1 + 2y), & -N \le y \le -1 \\ 1 - \dfrac{\omega}{2\alpha}y^2, & -1 \le y \le 1 \\ 1 + \dfrac{\omega}{2\alpha}(1 - 2y), & 1 \le y \le N \end{cases}; \tag{2.10}$$

$$\frac{\partial U}{\partial y} = \begin{cases} 0, & -N < y < -1 \\ \omega, & -1 < y < 1 \\ 0, & 1 < y < N \end{cases};$$

$$\frac{\partial H}{\partial y} = \begin{cases} \dfrac{\omega}{\alpha}, & -N \le y \le -1 \\ -\dfrac{\omega}{\alpha}y, & -1 \le y \le 1 \\ -\dfrac{\omega}{\alpha}, & 1 \le y \le N \end{cases}.$$

[Note that hereafter ω denotes the nondimensional shear—that is, the dimensional shear U_0/L, divided by f so ω is also the Rossby number $U_0/(fL)$—whereas both $u(y)$ and $V(y)$ denote the y-dependent, nondimensional amplitudes of the two velocity components.]

The condition $H(y) > 0$ for all y, including the walls ($y = \pm N$), is trivially satisfied for all $\omega < 0$ and translates into the constraint

$$1 + \frac{\omega}{2\alpha}(1 - 2N) > 0 \quad \Rightarrow \quad N < \frac{1}{2} + \frac{\alpha}{\omega}, \quad \text{for } \omega > 0. \tag{2.11}$$

At the boundaries of the inner zone, $y = \pm 1$, the normal velocity (and thus V, too) must be continuous, whereas the tangential velocity u has to undergo the following jump to ensure the continuity of η [due to the jump in U_y; see Eq. (2.6)]:

$$u_{-1+\varepsilon} = u_{-1-\varepsilon} - \omega \left.\frac{V}{U - C}\right|_{y=-1};$$
$$u_{1+\varepsilon} = u_{1-\varepsilon} + \omega \left.\frac{V}{U - C}\right|_{y=1}. \tag{2.12}$$

The boundary conditions at the two walls are the vanishing of the normal velocity component there, $V(y = \pm N) = 0$. As an arbitrary normalization of the problem we choose $u(y) = 1$ at either of the two walls; thus, if we choose $u(y = -NL) = 1$, the boundary conditions at $y = \pm NL$ are

$$V(y = \pm NL) = 0; \quad u(y = -NL) = 1. \tag{2.13}$$

Unstable solutions of system (2.9) subject to the boundary conditions (2.13) [and with the jump conditions (2.12)] have a nonvanishing imaginary part of the phase speed; that is, $C_i \neq 0$ when $C = C_r + iC_i$. Before turning to these unstable solutions of system (2.9), we note that with the above scaling, the nondivergent case is obtained formally from (2.9) by setting $H^{-1} = 0$. Dropping all terms with H in the denominator, letting $U_{yy} = 0$ in all three regions [see $U(y)$ in (2.10)], and separating u and V between Eqs. (2.9a) and (2.9b) yields $u_{yy} = k^2 u$ and $V_{yy} = k^2 V$. This is precisely the right form of Laplace's equation [given in the nondivergent case by Eq. (1.1)] for the assumed wavelike solutions of u and V in x: e^{ikx}. It should also be stressed that V is the streamfunction because the actual velocities are related to it via $u = -dV/dy$ and $v = ikV = dV/dx$. Because $V(y) = e^{\pm ky}$, regularity mandates that for $k^2 > 0$, V vanishes at $y = \pm\infty$, so we require that $V(y = \pm N) = 0$ for sufficiently large N.

3. Method of solution

The dispersion relations of the unstable modes were calculated by integrating (a fifth-order Runge–Kutta scheme with 10^{-10} tolerance was used to ensure accuracy) system (2.9) from one of the walls (say $y = -N$), starting with the initial conditions $V = 0$ and $u = 1$, to the southern boundary of the shear zone, $y = -1$. The continuity of V and the jump condition for u, Eq. (2.12), were then applied to cross to the intermediate shear zone at $y > -1$ and system (2.9) was integrated through the shear zone to the northern boundary of the shear zone, $y = +1$, where the same conditions of continuity of V and jump of u, Eq. (2.12), were applied again to cross to the northern outer region, $y > +1$. The integration of system (2.9) then proceeded from $y = +1$ to the northern wall, $y = +N$, and the value V was recorded. The value of $C = C_r + iC_i$ was changed to find the values for which $V(y = +N) = 0$. Many (complex as well as real) values of C were found in this way for any given values of k and α, but only the one with maximal C_i is reported here. The determination of the maximal value of kC_i for a given value of k follows an involved numerical search that uses both initial guesses from the prior k value and independent searches that begin from nine other pairs of (C_r, C_i) values. From each initial guess, the search employs a two-dimensional minimization algorithm that finds the simultaneous zeros of $\mathrm{Re}[V(y = N; C_r, C_i)]$ and $\mathrm{Im}[V(y = N; C_r, C_i)]$.

At large values of k and small values of α the variation of the eigenfunctions with y turned out to be too rapid and the growing exponential in the outer regions dominated the solutions, which made the numerical search for C extremely sensitive. In such cases two integrations of Eqs. (2.9) were initiated, each from one of the two walls, and the condition that determined C was the continuity of these two solutions at $y = 0$. At intermediate values of k and α, the two methods of direct integration from one wall to the other (requiring V to vanish at the other wall) and integrating from either of the walls to $y = 0$ (requiring the V and u solutions to be continuous at $y = 0$) resulted in the same values of C.

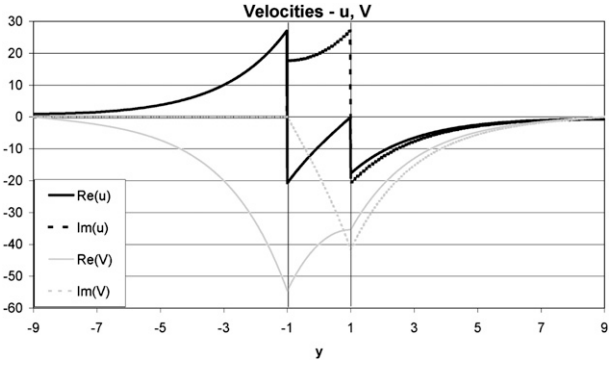

FIG. 3. The $u(y)$, $V(y)$ eigenfunctions for the ND case at $k = 0.5$. The vorticity, divergence, and height all vanish identically everywhere including the transition points $y = \pm 1$ (graphs not shown) because of the particular method of solution we use. The exponential decay in the two outer regions is expected from the analytical solutions in the unbounded case.

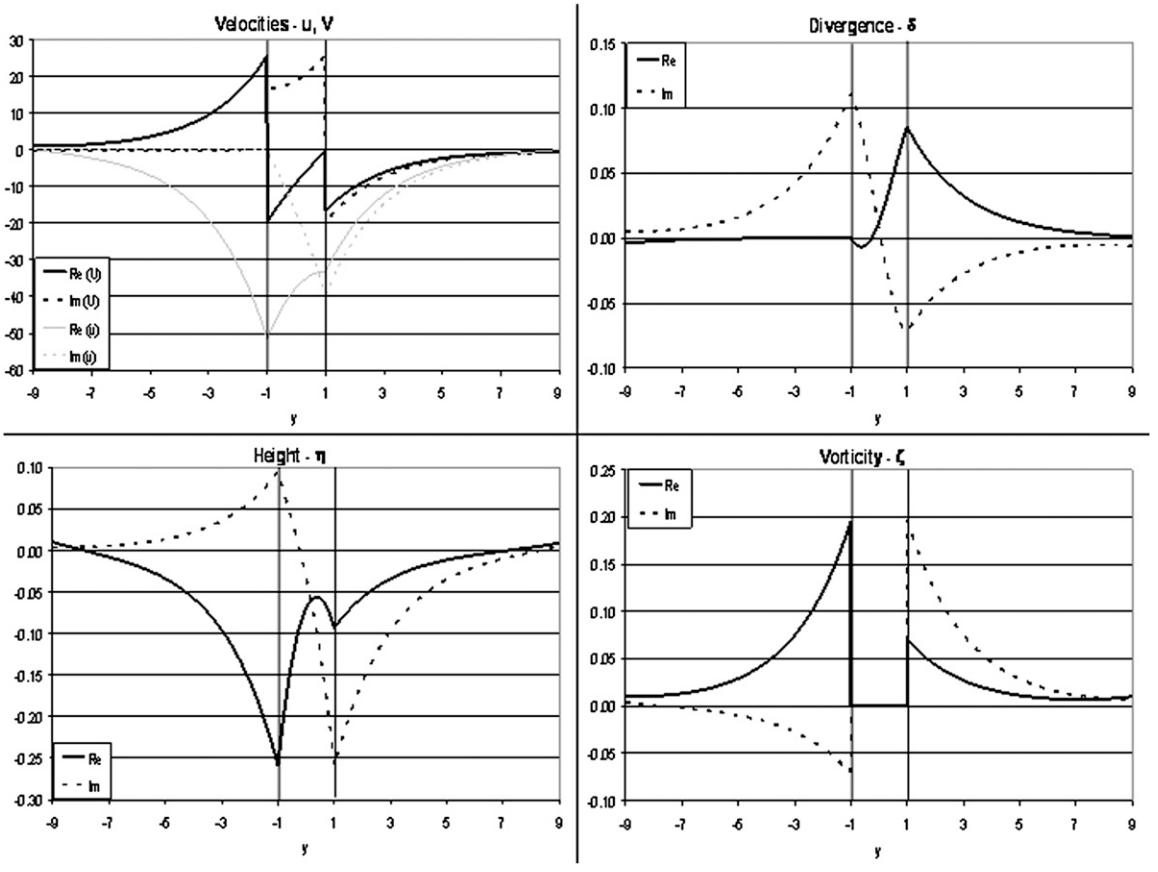

FIG. 4. Eigenfunctions for the divergent $\alpha = 100$, $\omega = 1$ case at $k = 0.5$. Also shown are the fields of height η, nonedge vorticity ζ, and divergence δ. The vorticity vanishes for $-1 < y < 1$, as expected for $\omega = 1$. The edge vorticity at $y = \pm 1$ is ignored in the vorticity panel.

The solutions of the nondivergent case were calculated by letting $H^{-1} = 0$ (i.e., setting to zero all terms with H in the denominator) as well as $U_{yy} = 0$ in the coefficients of system (2.9). Analytically, this procedure yields exactly Laplace's Eq. (1.1) for V ($\equiv \psi$ because $v = ikV$).

The meridional structures of vorticity ζ and divergence δ were calculated from the solutions $u(y)$ and $V(y)$ $[=-iv(y)/k]$ solutions of system (2.9) via the relations

$$\zeta = \frac{\partial v}{\partial x} - \frac{\partial u}{\partial y} = -k^2 V - u_y, \tag{3.1a}$$

$$\delta = \frac{\partial u}{\partial x} + \frac{\partial v}{\partial y} = iku + ikV_y = ik(u + V_y), \tag{3.1b}$$

while the height structure was calculated from the nondimensional counterpart of Eq. (2.6a):

$$\eta = -\frac{1}{\alpha}[u(U - C) + V(U_y - 1)]. \tag{3.1c}$$

In the nondivergent case $1/H$ is set equal to 0, so setting $1/\alpha = 0$ in (3.1c) guarantees that η vanishes at all times, whereas δ and ζ vanish because of their dynamics.

4. Unstable modes and growth rates

In all the calculations reported below, the value of N in Eq. (2.13) [i.e., half the region over which system (2.9) was integrated] was chosen to be 9. This ensures that the imposition of the condition $V(y = \pm N) = 0$ filters out the exponentially growing $V(y)$ from the solution in the outer regions and, as argued in section 1, it is within the unstable range of the bounded nondivergent case ($N > 2$). A numerical reproduction of the analytical nondivergent dispersion curve of the unstable modes is shown in Fig. 2 (solid curve designated as ND) along with the corresponding curve (dashed) of divergent perturbation for $\alpha = 100$ and $\omega = 1$. The numerically generated ND curve is an exact reproduction of the theoretical expression (1.2), which confirms both the accuracy of the numerical method outlined in section 3

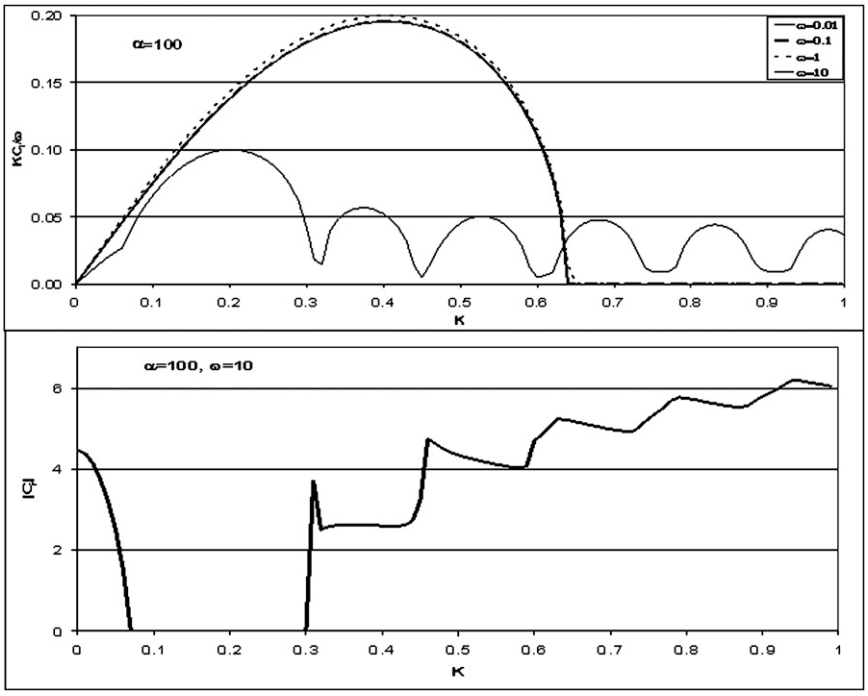

FIG. 5. Shear effects for $\alpha = 100$ and $\omega = 0.01, 0.1, 1.0$, and 10.0. The new shear mode at $\omega = 10$ does not have a shortwave cutoff at $O(1)$ wavenumber and its maximal growth rate is only a bit smaller than that of the low shear (and ND) modes. Note that the growth rate curves for $\omega = 0.1$ and $\omega = 0.01$ can hardly be distinguished from one another and that their maximal scaled growth rate is actually smaller than for $\omega = 1$. The (top) jumps in the kC_i curves are correlated with the (bottom) jumps in C_r.

and the validity of our choice of $N = 9$ for representing the unbounded outer regions. A slight difference between the divergent and nondivergent curves can be noticed near the cutoff wavenumber $k = 0.639$, where the former extends to slightly larger wavenumbers (shorter wavelengths) than the latter. The choice of ω in the divergent case (in the nondivergent case it is a trivial multiplicative factor) follows from condition (2.11), which ensures that the fluid thickness does not vanish. It implies that $\omega < \alpha/(N - \frac{1}{2})$ so that for $N = 9.0$ it is fully satisfied by selecting $\omega \leq \alpha/10$, a condition satisfied in all calculations reported below.

The close similarity between the two curves confirms that when the radius of deformation, $L\alpha^{1/2} = (gH_0)^{1/2}/f$, is large (10 times L, the width of the shear zone), the divergent instability curve is accurately approximated by the nondivergent curve. However, the closeness of the instability curves does not guarantee closeness of the corresponding eigenfunctions and in particular, the exponential decay of the nondivergent eigenfunctions in the outer regions.

Figure 3 shows the u, V eigenfunctions of the nondivergent flow perturbations. The exponential decay in the outer regions is quite obvious, as expected from the analytic solution. The corresponding vorticity and divergence (not shown) both vanish everywhere, including at $y = \pm 1$ because our method of solution does not capture the vorticity δ-function structure there. In contrast, Fig. 4 shows the corresponding eigenfunctions, as well as vorticity and divergence, for the divergent flow, from which it is evident that even though the $u(y)$, $V(y)$ fields are very similar to those of nondivergent flows, the vorticity and divergence are maximal at the transition points, where their values are small compared to, say, ku or kV, but they do not vanish at $y \neq \pm 1$. We should emphasize that because the $u(y)$ and $V(y)$ fields are not calculated at $y = \pm 1$, the vorticity field ζ shown in Fig. 4 (and in Figs. 6, 7, 9, 12 below) represents only the nonedge vorticity, whereas the edge δ-function vorticity associated with the jump discontinuity of U_{yy} at $y = \pm 1$ is not captured by our solution.

The separate effects of changing ω and decreasing α (called shear effects and radius-of-deformation effects, respectively) are studied next by changing the value of one of them and examining the resulting effects on the eigenfunctions and vorticity/divergence fields.

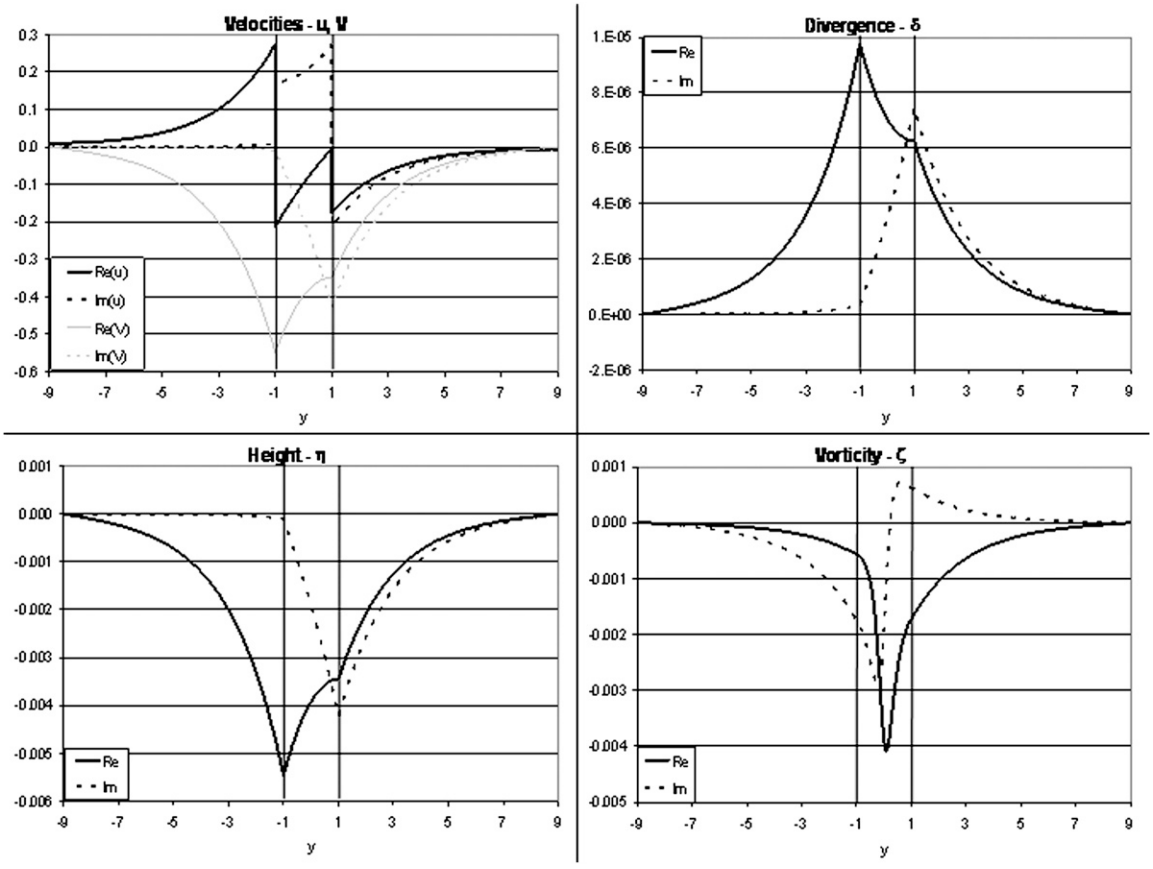

FIG. 6. The eigenfunctions at $\alpha = 100$ and $k = 0.5$ of the low shear mode: $\omega = 0.01$. The $u(y)$ and $V(y)$ eigenfunctions are similar (in both inner and outer regions) to those at $\omega = 1$ (see Fig. 4). However, the height, nonedge vorticity, and divergence are quite different than those at $\omega = 1$: the divergence does not cross zero, the nonedge vorticity is maximal inside the inner region (and not at $y = \pm 1$), and the height is real at $y < -1$.

a. Shear (Rossby number) effects

For nondivergent flows, Eq. (1.2) affirms that changing the mean shear $\omega = U_0/(fL)$ (which is also a Rossby number of the mean flow) only changes the magnitude of the growth rate curve but not its k dependence. To conform to the ND independence on ω, all growth rate curves in the figures of this study show kC_i/ω as a function of k, so the direct ω effect on the amplitude is filtered out. At values of ω other than 1.0, the growth rate curves of Fig. 2 are modified into those shown in Fig. 5, where the value of α is set to 100 in all cases. For values of $\omega \leq 1$, the growth rate curves differ only slightly modified from those of ND, and the normalized growth rates increases very slightly with ω (the dotted $\omega = 1$ curve is slightly above the two $\omega < 1$ curves). We note that although these results are natural in the quasigeostrophic theory (large radius of deformation and Rossby number smaller than 1), the streamfunction in the QG theory is the height, that is, $V = \alpha\eta$ in our notation, which is not the case here as is evident from Fig. 4 (see also Fig. 6).

In contrast, for $\omega = 10$ a new mode of instability can be clearly noticed in the growth rate curves; it does not have a shortwave cutoff and its maximal growth rate (divided by ω) is about half that of the other cases. The lower panel in Fig. 5 shows that the different lobes of this high-shear instability are associated with coalescence of different real-mode modes as in Paldor and Ghil (1991). The corresponding eigenfunctions shown in Fig. 6 for $\omega = 0.01$ (and $k = 0.5$) are also fairly similar to those of the $\omega = 1$ eigenfunctions (see Fig. 4) and the same is true for the height, vorticity, and divergence fields (see Fig. 4). In agreement with the drastic change in growth rate curves, the eigenfunctions of the new mode, shown in Fig. 7, differ significantly from those of the former cases—they do not decay to zero in the outer regions and the vorticity and divergence associated with this unstable mode do not attain their maximal values near the transition points $y = \pm 1$. A possible

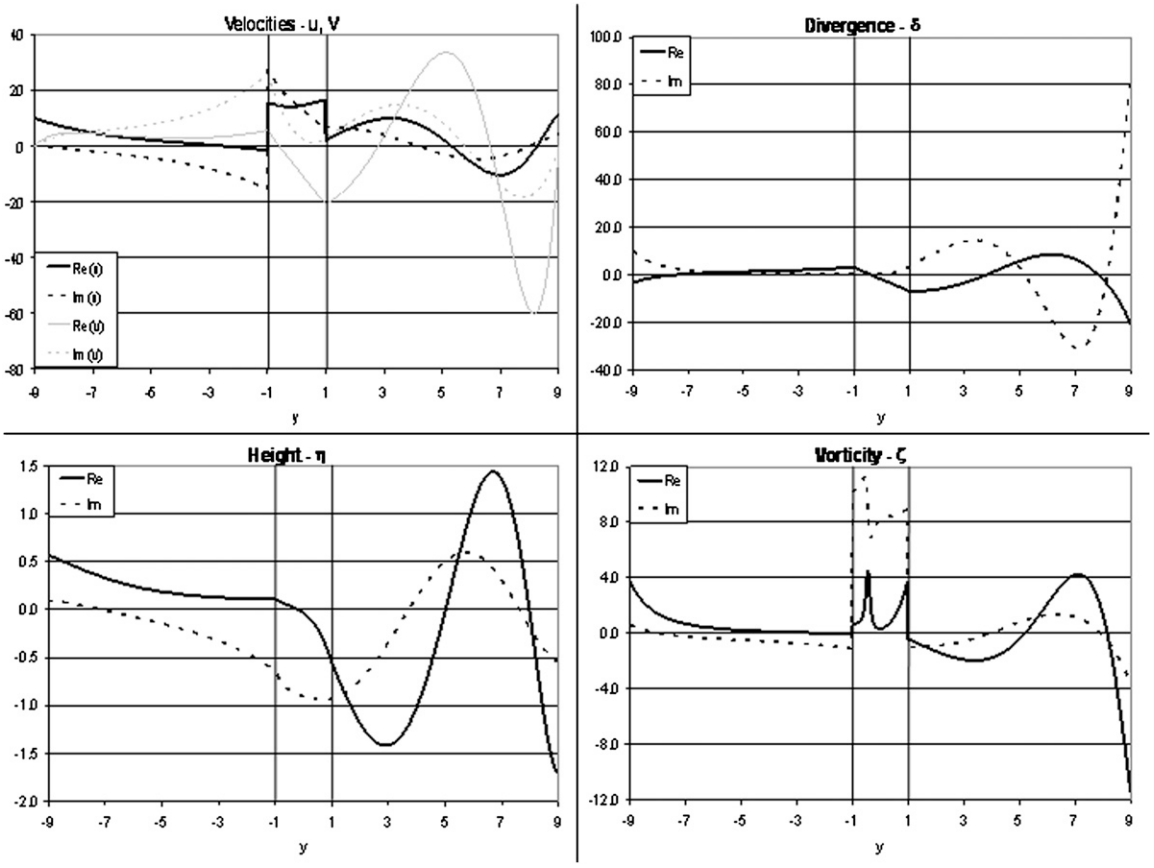

FIG. 7. The eigenfunctions at $\alpha = 100$ and $k = 0.5$ for the high shear effect, $\omega = 10$. The effect of the high shear is clear in structure of $u(y)$ and $V(y)$ eigenfunctions that do not decay to zero in the outer regions while the height, nonedge vorticity, and divergence are maximal in the outer region.

interpretation of these large Rossby number modes is given in the discussion and summary section.

b. Radius of deformation effects

For the large value of $\alpha = 100$ studied in the previous subsection, the condition (2.11) was satisfied at all values of $0.01 < \omega < 10$. However, any decrease of the value of α mandates a decrease in the value of ω (e.g., $\omega < \alpha/10$) to guarantee that condition (2.11) is satisfied. The growth rate curves shown in Fig. 8 were calculated for values of α of 0.1, 1.0, 10 and 100, so the (fixed) value of ω was set to 0.01 to ensure that condition (2.11) is satisfied even at the lowest value of $\alpha = 0.1$. As in all other growth rate curves in this study, the ordinate is kC_i/ω to account for the direct multiplicative effect of ω on the growth rates. It is clear from these curves that the effect of decreasing the radius of deformation (for fixed shear zone width) is different for long waves and short waves. Whereas the growth rate curves diminish with α for long waves, at wavenumbers slightly above the cutoff ($k = 0.639$; i.e., $0.639 < k < 0.7$) the growth rates become nonzero when α gets smaller. The corresponding changes in the eigenfunctions are summarized in Fig. 9 for $\alpha = 0.1$ (so $\omega = 0.01$) and $k = 0.5$. The $u(y)$, $V(y)$ structures are significantly different from those shown in Fig. 4 and they vary quite abruptly inside the inner, linear shear region. This sharp variation in the inner region is strongly reflected in the vorticity that undergoes a double delta-like flip-flop near $y = 0$ ($0 < y < 0.02$).

c. Cyclonic mean shear

The results shown in the preceding two subsections are concerned with anticyclonic mean (relative) vorticity: $\omega > 0$. In contrast to the nondivergent problem, the sign of ω (as well as its value, as shown above) affects the solutions in the present divergent problem. The calculations of section 4a were repeated for negative ω values and we found that (as was the case for the value of ω for $\omega > 0$) the longwave, nondivergent instability is only slightly affected by the change of the sign of ω. In Fig. 10 we compare the growth rate curves for $\alpha = 0.1$ and for two values of $\omega = +0.01$ (shown in the $\alpha = 0.1$

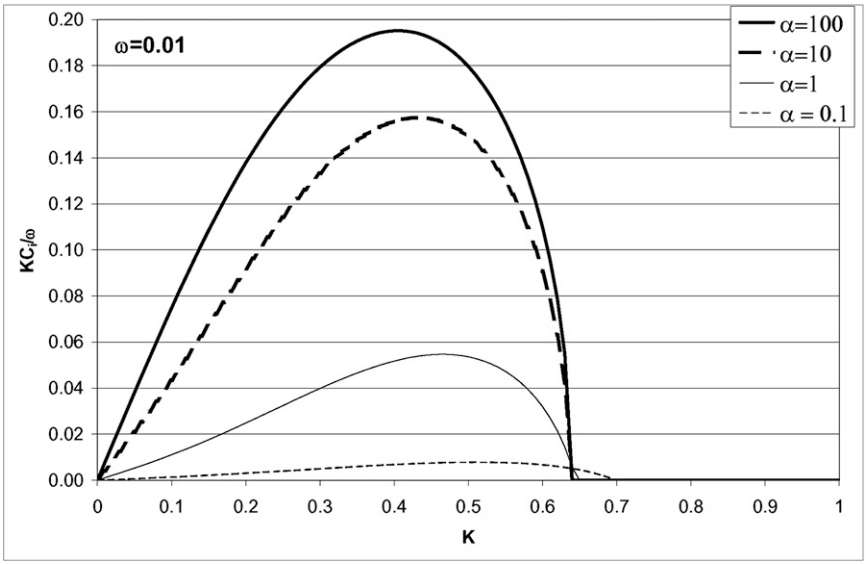

FIG. 8. Growth rate curves for the radius-of-deformation effect for $\omega = 0.01$ and $k = 0.5$ and for the indicated values of $\alpha = 0.1$, 1, 10, and 100 (i.e., $\omega \leq \alpha/10$ even for the lowest value of $\alpha = 0.1$). The decrease in maximal growth rate kC_i/ω (beyond the scale factor of ω) is clearly evident when α is decreased, along with a slight extension of the shortwave cutoff to higher wavenumber values.

curve of Fig. 8) and $\omega = -0.01$. The difference between the two curves decreases with the increase in α, and at $\alpha = 100$ the difference is smaller than the line width. However, insofar as the new shortwave mode is concerned the difference between positive and negative ω is more dramatic. Figure 11 shows a comparison between the growth rate curves for $\alpha = 100$; $\omega = +10$ (see the $\omega = 10$ curve in Fig. 5a) with that for $\alpha = 100$; $\omega = -10$. It is clear from these results that no longwave limit exists for cyclonic mean shear and that the undulations of the growth rate curve are slower and smoother than those for anticyclonic mean shear. As Fig. 12 shows, the eigenfunctions of this case are also markedly different from those of $\omega = +10$ shown in Fig. 7.

In contrast to anticyclonic mean shear where small values of $\alpha/|\omega|$—i.e., large values of $|\omega|/\alpha$—violate condition (2.11) as the mean height becomes negative at the walls, for $\omega < 0$ $H(y)$ never vanishes in the outer regions; that is, according to the $\partial H/\partial y$ equation in (2.10) it increases monotonically there with the distance from the inner region. Therefore, it is not a priori clear if instabilities exist for, say, $\alpha = 1$ and $\omega = -10$ (for which a positive ω counterpart does not exist). Although large negative mean shears are not the most relevant to geophysical shear flows (Ford 1994), for completeness of the analysis we investigate their instability as well. Our intensive numerical search that uses the exact same method as in the rest of this study has not yielded any instability in the cases we have examined: $\alpha = 1$ and $\omega = -1$ and $\alpha = 10$ and $\omega = -10$ (in addition to $\alpha = 1$ and $\omega = -10$). This intensive search was extended to wavenumbers larger than 1 (up to $k = 2$), but no instabilities were found. A confirmation of our finding regarding the stable nature of the perturbation at these values of ω and α might be sought in direct numerical solutions of the initial value problem starting from a spatially concentrated perturbation. However, this requires one to solve numerically partial differential equations (PDEs), so the simplicity and accuracy of numerical solution of linear eigenvalue equations is lost.

5. Discussion and summary

The numerical results presented above reproduce with high accuracy the analytical results of the unbounded ND case, which lends credence to our numerical procedure and confirms our choice of $N = 9$ as the "infinity" limit of the outer regions.

A comparison between the ND and divergent solutions shows that the former are accurate approximations of the latter only when the radius of deformation ($L\alpha^{1/2}$) is at least one order of magnitude larger than the width of the linear shear zone ($2L$) and provided the vorticity of the mean shear (U_0/L) does not exceed the planetary vorticity (f) (i.e., the Rossby number is smaller than 1). We note that the Froude number is $U(gh)^{-1/2} = \omega\alpha^{-1/2}$, which is independent of f and can be less than unity provided α (the radius of deformation) is large. For small

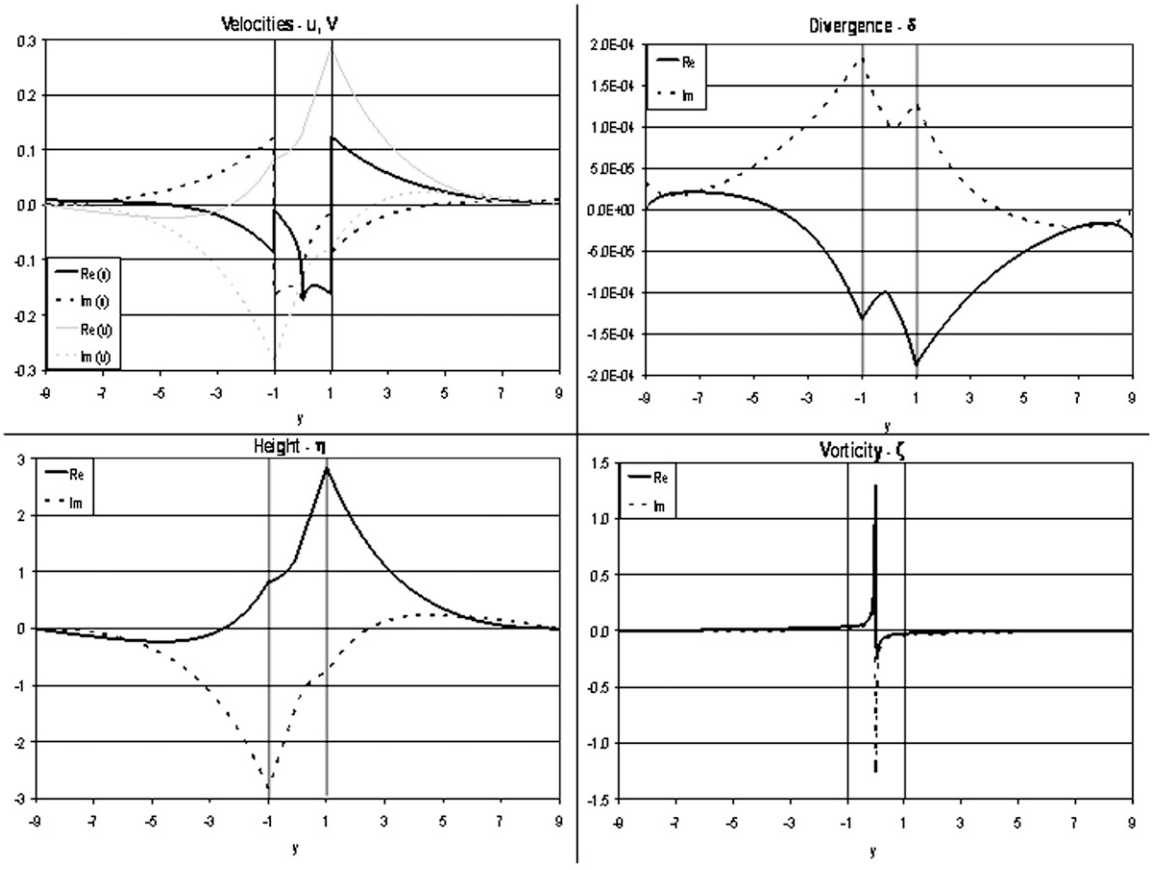

FIG. 9. The eigenfunctions for small radius of deformation, $\alpha = 0.1$, $\omega = 0.01$ ($= \alpha/10$), and $k = 0.5$. The nonmonotonic variation of the $u(y)$ and $V(y)$ velocity components is quite obvious in comparison to Fig. 4 and Fig. 6 and the nonedge vorticity maximum at $y = 0$ stands out in comparison to all other cases shown above.

deformation radii and for large Rossby numbers (mean shear significantly larger that the planetary vorticity), new modes exist that cannot be captured by the ND dynamics.

The irrelevance of ND instability dynamics to divergent instability is most pronounced for short waves ($k > 0.64$) where the solutions of the former problem are all stable whereas the latter have instabilities that are comparable to (about half) the longwave ND maximum instabilities.

On the other hand, in the $\omega = 1$ case and for sufficiently large deformation radius, the ND theory should provide a good approximation for divergent perturbations. The reason is that for $\omega = 1$, Fig. 4 shows that vorticity in the inner region vanishes just as in the ND case (where it vanishes everywhere). The vorticity perturbation that has a delta-function distribution at $y = \pm 1$ (which cannot be captured by our numerical method) in the ND case becomes maximal at these points for the case shown in Fig. 4. For zonally propagating waves, the vorticity evolution equation (derived from cross differentiation of the x and y momentum equations) yields

$$(U - C)\zeta = VU_{yy} + (1 - U_y)(i\delta/k), \qquad (5.1)$$

where the vorticity ζ and divergence δ are defined in Eq. (3.1). In both the ND and $\omega = 1$ (so $1 - U_y = 0$ in the inner region) cases, the divergence (second) term on the rhs of Eq. (5.1) vanishes in the inner region, so vorticity can only be generated there by the edge term VU_{yy} (i.e., by meridional advection of mean vorticity gradient away from $y = \pm 1$). This consideration explains the vanishing of perturbation vorticity in the inner region for $\omega = 1$ (Fig. 4) as in the ND case. In contrast, when $\omega \neq 1$, significant vorticity is generated in the inner region (Fig. 6, $\omega = 0.01$; Fig. 7, $\omega = 10$; and Fig. 9, $\omega = 0.01$ where the vorticity is singularly large in this region).

The present study only illuminates some of the subtle issues encountered when divergence is introduced into the dynamics. An analysis of the results presented here must therefore begin by transforming the set (2.5) into the corresponding set for the perturbation vorticity ζ,

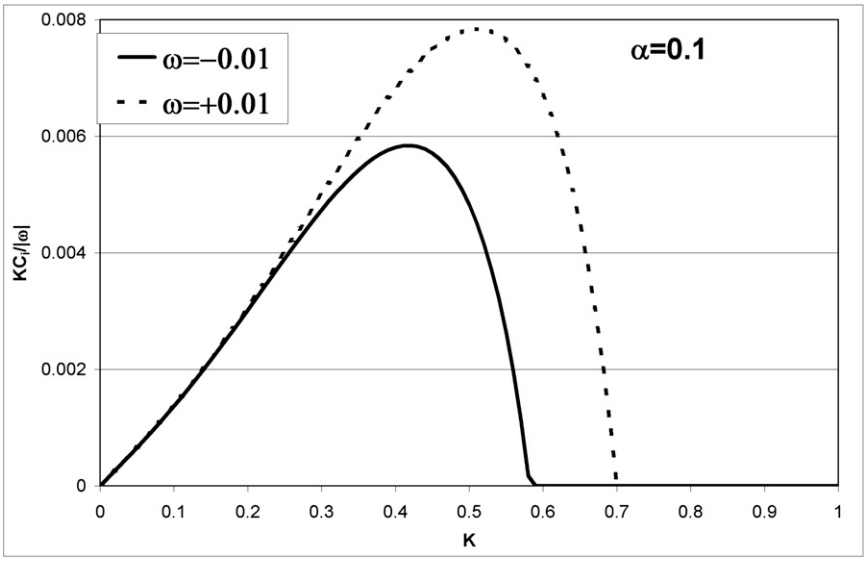

FIG. 10. A comparison between the growth rate curves at $\omega = +0.01$ and $\omega = -0.01$ for $\alpha = 0.1$. The instability for cyclonic mean shear is smaller and occupies a narrower wavelength range than that of anticyclonic mean shear.

elevation η, and divergence δ. Here we only provide a rather rudimentary interpretation of the findings of this work and leave a fuller analysis to future works. The nondimensional (using the scaling adopted above) evolution equations for these variables (derived by taking the divergence and curl of the momentum equations) are

$$\frac{D\zeta}{Dt} = \omega[\delta^{y+1} - \delta^{y-1}]v + \delta(U_y - 1), \tag{5.2a}$$

$$\frac{D\delta}{Dt} = \zeta - 2U_y v_x - \alpha\nabla^2\eta, \tag{5.2b}$$

$$\frac{D\eta}{Dt} = -H\delta + \frac{U}{\alpha}v, \tag{5.2c}$$

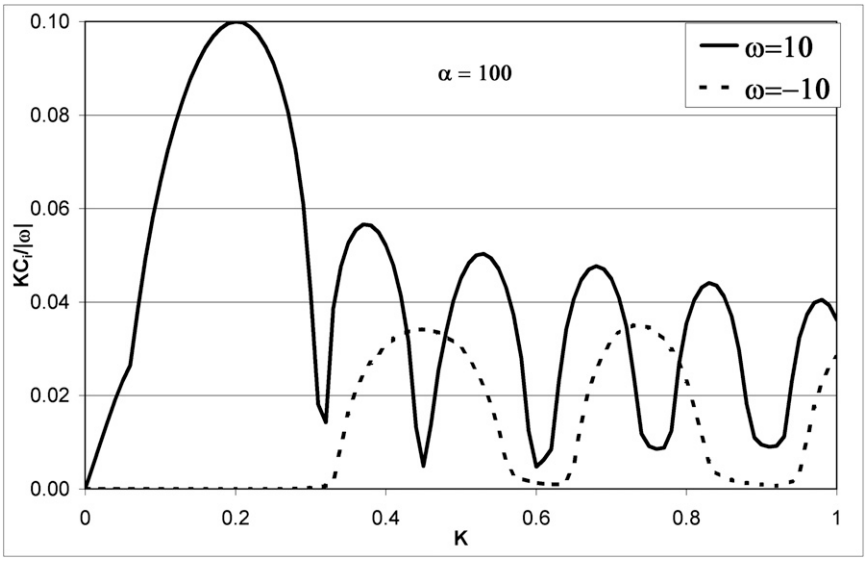

FIG. 11. A comparison between the shortwave instability at $\omega = +10$ and $\omega = -10$ for $\alpha = 100$. The main difference between the two is the absence of a longwave branch at $\omega = -10$ and the slower rate of change of kC_i with k for this cyclonic mean shear.

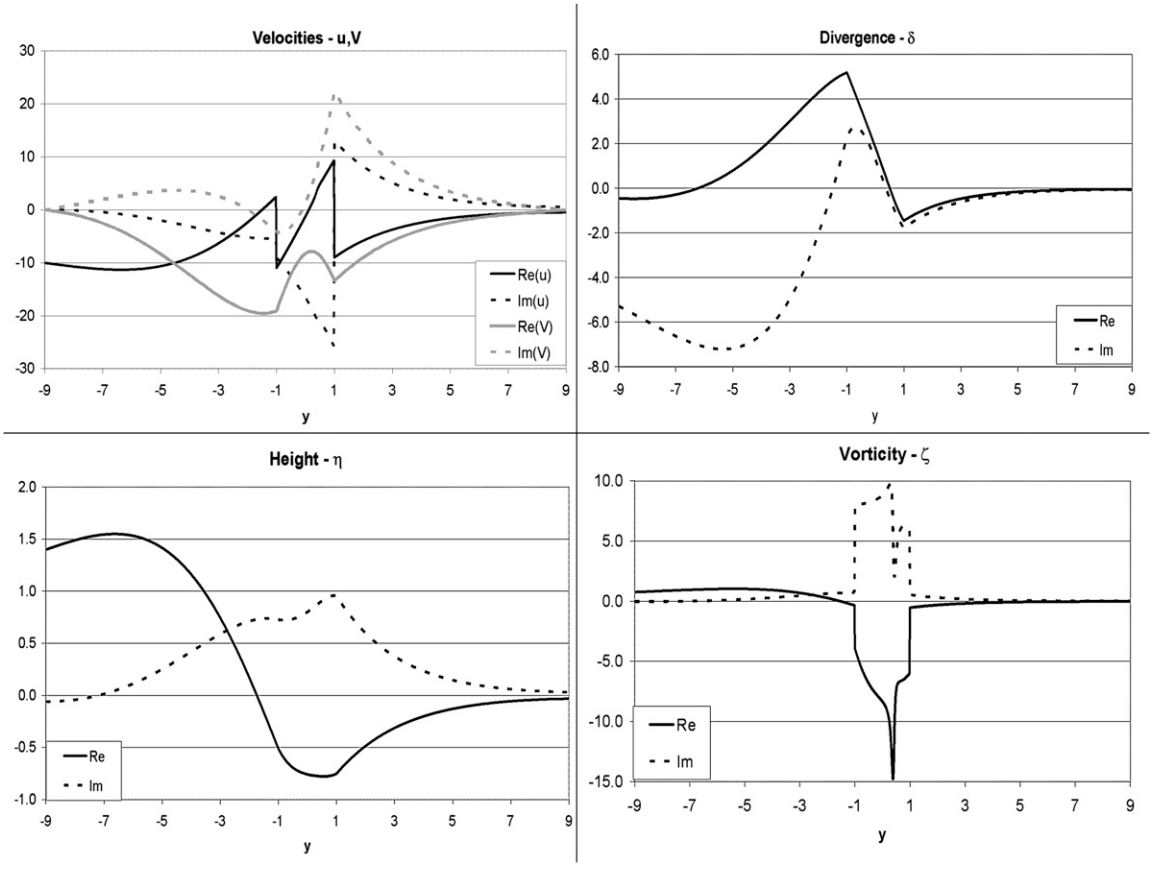

FIG. 12. The eigenfunctions for $\alpha = 100$, $\omega = -10$, and $k = 0.5$, which is the counterpart of those shown in Fig. 7 for anticyclonic mean shear.

where the definitions of ζ, η, and δ are given in (3.1) and where $D/Dt = \partial/\partial t + U\partial/\partial x$ as before.

The terms in the square bracket in (5.2a) that have δ with superscripts $y + 1$ and $y - 1$ designate the δ function that vanishes everywhere except for $y = -1$ and $y = +1$, respectively (and whose integral over the entire real axis is 1), and should not be confused with the divergence (designated here by δ). These terms result from the discontinuity of the mean vorticity at $y = \pm 1$. The nondivergent case is obtained from (5.2) by setting $\delta = 0$, in which case the set (5.2) is overdetermined, being a set of three equations for two unknowns (ζ and η). However, for $\alpha^{-1} = 0$ (infinite deformation radius) Eq. (5.2c) is satisfied by $\eta = 0$ but Eq. (5.2b) is ill defined because $\alpha\nabla^2\eta = \nabla^2\eta/\alpha^{-1}$, which cannot be evaluated (zero divided by zero). Ignoring these issues of consistency between the shallow water model (SWM) and ND dynamics, the latter is fully and solely described by Eq. (5.2a), which reduces to

$$\frac{D\zeta}{Dt} = \omega(\delta^{y+1} - \delta^{y-1})v, \tag{5.3a}$$

where

$$\zeta = \nabla^2\psi, \quad v = \psi_x. \tag{5.3b,c}$$

For this limiting case, Heifetz et al. (1999) showed that the normal mode dynamics can be fully described in terms of action-at-a-distance interaction between the two δ-function vorticity waves centered on $y = \pm 1$. For this nondivergent case, the modal growth is enabled by two edge waves having the same amplitude, but the phase of the northern wave (the one centered on $y = +1$) is shifted by an angle between 0 and π to the left (westward) relative to the phase of the southern wave (the one centered on $y = -1$). Each of these edge waves is a Rossby wave that propagates in the opposite direction to the mean flow at its center (eastward at $y = -1$ and westward at $y = +1$) and the speed of the counterpropagation is proportional to the wavelength. Modal growth occurs when the phases of two waves are locked, which for long waves mandates that the action-at-a-distance interaction hinders their counterpropagation so the phase shift should be between $\pi/2$

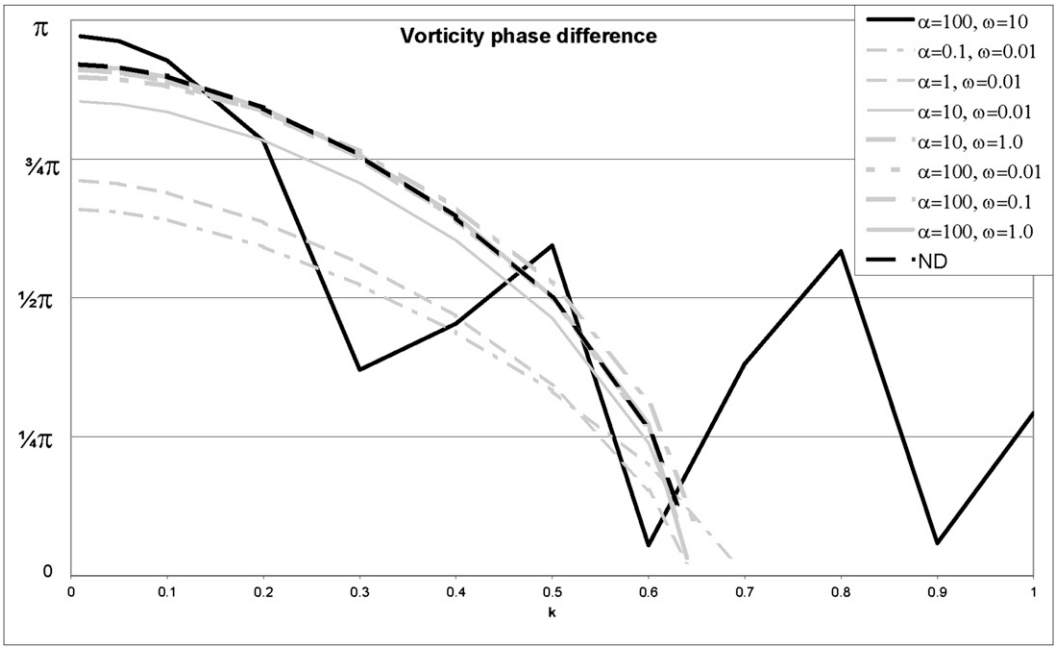

FIG. 13. Phase difference of vorticity across the shear zone, $y = +1$ and $y = -1$, as a function of k for the ND case and for the divergent cases calculated in this study. In all cases with $\omega \leq 1$ the numerical results are close to the theoretical ND values: between $\pi/2$ and π for long waves ($k \to 0$) and between 0 and $\pi/2$ for short waves ($k \to 0.7$). For the large Rossby mode $\omega = 10$ the phase difference is not monotonic with k, in accordance with the instability curve of Fig. 5.

and π, whereas for short waves the action-at-a-distance interaction speeds up the counterpropagation so the phase shift should be between 0 and $\pi/2$.

Although the dynamics associated with (5.2) is far more complex than that of (5.3), it is still affected by the δ-function edge waves, as is evident from the presence of the $\delta^{y+1} - \delta^{y-1}$ term in (5.2a). In Fig. 13 we compare the variation of the phase shift between the two vorticity edge waves with wavenumber in the ND case and in several divergent cases calculated in section 4 (i.e., the phase shift of the two edge vorticities that were neglected in Figs. 4, 6, 7, 9, and 12). The phase shift of divergent flows is similar to that of the ND case, especially at large deformation radius ($\alpha = 100$), as long as $\omega \leq 1$, which reflects the overall similarity between the instability curves of Fig. 8. In contrast, at $\omega = 10$ the variation of the phase shift with wavenumber is nonmonotonic, as is the growth rate curve in Fig. 5a.

It should be emphasized that these straightforward vorticity considerations of the interaction between vorticity edge waves do not provide a complete description of the dynamics. To show this, we derive the evolution equation for the linearized Ertel potential vorticity (PV) $q = \zeta + \eta H^{-1}(U_y - 1)$ (strictly speaking, the linearized Ertel PV is qH^{-1}), either directly from its (Lagrangian) conservation or by combining Eqs. (5.2a) and (5.2c):

$$\frac{Dq}{Dt} = \left[\omega(\delta^{y+1} - \delta^{y-1}) + \frac{U}{\alpha H}(U_y - 1)\right]v. \quad (5.4)$$

Because $U(y = 0) = 0$, the mean PV gradient on the rhs of this equation vanishes there. Therefore, for growing modes the PV perturbation vanishes at $y = 0$ [i.e., $q(y = 0) = 0$] but for $\omega < 1$ the vorticity perturbation ζ is nonzero and is positively correlated with the displacement perturbation [$\zeta = (1 - \omega)\eta$] there. Positive (cyclonic) vorticity circulating positive height anomaly is an indication or the existence of inertia–gravity waves at the center of the shear layer that interact with the two Rossby edge waves. This interaction is eliminated in ND where the inertia–gravity waves have infinite phase speed (or infinite radius of deformation). When $\omega = 1$, Eq. (5.2a) reduces to its ND form (5.3a) within the shear region so the vorticity vanishes throughout this region. Therefore, for $\omega = 1$ inertia–gravity waves are practically eliminated from the vorticity dynamics (see lower right panel in Fig. 4) and the agreement of the growth rates with those of the ND theory (Fig. 2) is nearly perfect. In all cases where the Froude number $\mathrm{Fr} = \omega\alpha^{-1/2}$ is small, Fig. 13 indicates that the instability is dominated by the

interaction between Rossby edge waves. This conclusion agrees with the results reported by Balmforth (1999) on the dominance of inflectional instability at small Fr and extends them to rotating flows. In the cases where Fr is $O(1)(\alpha = 100, \omega = 10)$, the C_r curve in Fig. 5 shows that the singular critical level may exist within the shear layer. Figure 13 and the mode structure (see Figs. 7 and 12) suggest that the ''super-sonic'' critical level instability is governed by inertia–gravity wave interaction, which is also in agreement with the results of Balmforth (1999) for nonrotating flows. Thus, in the ND case the piecewise linear shear profile of Fig. 1 filters out the effects of both inertia–gravity waves and singular critical levels, leaving the Rossby inflectional instability as the sole destabilizing mechanism.

The results presented in this study support the previous results reported by Paldor and Dvorkin (2006), who extended numerically the classical barotropic instability theory for ND perturbations on a zonal jet on the β plane (i.e., Kuo 1973) to divergent perturbations. Similarly to the findings in the present Rayleigh problem, in Kuo's barotropic instability problem the ND instabilities approximate the divergent quite poorly, and especially so in the shortwave range where ND perturbations are stable whereas divergent perturbations have large growth rates. Our results extend to rotating flows on the f plane the nonrotating results of Balmforth (1999) and show that even in the small Froude number regime the instability is affected by the value of the deformation radius such that when it increases the growth rates decrease and shift to smaller wavelengths (Fig. 8). The nonsmooth supersonic instability at Fr of order 1 with no shortwave cutoff is similar to the instability found by Paldor and Ghil (1991) in two-layer geostrophic coastal fronts for sufficiently fast mean currents. A deeper analysis should be carried out to unravel the physics involved with this supersonic instability of the Rayleigh problem (e.g., overreflection and WKB expansion in the $\omega - 1 \rightarrow 0$ limit).

Acknowledgments. This work was supported by Grant 579/05 of the Israel Science Foundation, by Grant 2006296 of the U.S.–Israel Bi-National Science Foundation to HU (NP) and by Grant 2004087 of the U.S.–Israel Bi-National Science Foundation to TAU (EH). We thank two anonymous reviewers for their very helpful, valuable, and constructive comments.

REFERENCES

Balmforth, N. J., 1999: Shear instability in shallow water. *J. Fluid Mech.,* **387,** 97–127.

Case, K. M., 1960: Stability of inviscid plane Couette flow. *Phys. Fluids,* **3,** 143–148.

Cushman-Roisin, B., 1994: *Introduction to Geophysical Fluid Dynamics*. Prentice Hall, 320 pp.

Drazin, P. G., and W. H. Reid, 1981: *Hydrodynamic Stability*. Cambridge University Press, 525 pp.

Farrell, B. F., 1988: Optimal excitation of perturbations in viscous shear flow. *Phys. Fluids,* **31,** 2093–2102.

Feng, M., and S. Wijffels, 2002: Intraseasonal variability in the South Equatorial Current of the east Indian Ocean. *J. Phys. Oceanogr.,* **32,** 265–277.

Ford, R., 1994: The instability of an axisymmetric vortex with monotonic potential vorticity in rotating shallow water. *J. Fluid Mech.,* **280,** 303–334.

Heifetz, E., C. H. Bishop, and P. Alpert, 1999: Counter-propagating Rossby waves in the barotropic Rayleigh model of shear instability. *Quart. J. Roy. Meteor. Soc.,* **125,** 2835–2853.

Kuo, H. L., 1973: Dynamics of quasi-geostrophic flows and instability theory. *Adv. Appl. Mech.,* **13,** 247–330.

Paldor, N., 2008: Non-divergent 2D vorticity dynamics and the shallow water equations on the rotating earth. *IUTAM Symposium on Hamiltonian Dynamics, Vortex Structures and Turbulence: Proceedings of the IUTAM Symposium Held in Moscow, 25–30 August 2006,* A. V. Borisov et al., Eds., IUTAM Book Series, Vol. 6, 177–187.

——, and M. Ghil, 1991: Shortwave instabilities of coastal currents. *Geophys. Astrophys. Fluid Dyn.,* **58,** 225–241.

——, and Y. Dvorkin, 2006: Barotropic instability of a zonal jet: From nondivergent perturbations on the β plane to divergent perturbations on a sphere. *J. Phys. Oceanogr.,* **36,** 2271–2282.

Pedlosky, J., 1987: *Geophysical Fluid Dynamics*. Springer-Verlag, 710 pp.

Pratt, L. J., and J. Pedlosky, 1991: Linear and nonlinear barotropic instability of geostrophic shear layers. *J. Fluid Mech.,* **224,** 49–76.

Satomura, T., 1981: An investigation of shear flow instability in a shear flow. *J. Meteor. Soc. Japan,* **59,** 148–167.

Send, U., 1989: Vorticity and instability during flow reversal on the continental shelf. *J. Phys. Oceanogr.,* **19,** 1620–1633.